

Development of an architecturally comprehensive database of forearm flexors and extensors from a single cadaveric specimen

Zhi Li^{a*}, Jeremy P.M. Mogk^{b1}, Dongwoon Lee^{c2}, Jacobo Bibliowicz^{b3} and Anne M. Agur^{a4}

^aDivision of Anatomy, Department of Surgery, University of Toronto, 1 Kings College Circle, Room 1158, Toronto, Ontario, Canada M5S 1A8; ^bEnvironment and Ergonomics Research Group, Autodesk Canada Inc., 210 King Street East, Toronto, Ontario, Canada M5A 1J7;

^cDepartment of Computer Science, University of Toronto, 40 St George Street, Toronto, Ontario, Canada M5S 2E4

(Received 5 June 2013; accepted 20 November 2013)

Technology has markedly improved the data that are used to generate musculoskeletal models; however, the need for more detailed musculotendinous architectural data persists. To address this need, we have digitised three-dimensional (3D) coordinate data of the fibre bundles (FBs) throughout the volumes of all 20 forearm muscles to generate a comprehensive database of the musculotendinous anatomy. The computerised reconstruction of the forearm anatomy enabled us to quantify muscle architectural parameters, as well as to visually examine the intricate spatial relationships between muscles and the 3D arrangement of FBs relative to their tendons and the underlying skeleton. The muscles of the forearm exhibited a wide range of architectural variation that we quantified using 3D geometric principles. This database improves upon that of previous studies and facilitates more detailed description of the muscle architecture in a format that can be used to inform and advance the development of state-of-the-art dynamic models for biomechanical simulations.

Keywords: muscle architecture; three-dimensional muscle modelling; digitisation; computational geometry; skeletal muscle; forearm

1. Introduction

Simulation of the musculoskeletal system is integral to understanding how the various muscles behave to move the skeleton in normal and pathological states. A wide range of disciplines, from computer science to medicine, require detailed three-dimensional (3D) anatomical models for simulation. The fidelity of these simulations depends on the accuracy of the data that are used to construct the models (Blemker et al. 2007; Lee et al. 2009). Traditional biomechanical models of the musculoskeletal system often use simplified geometry, where muscles are represented using a series of line segments to approximate each muscle's path geometry or effective line of action. Although these simplified representations might be sufficient for parallel-fibred muscles (e.g. biceps brachii), these models are limited in their ability to capture the contractile behaviour of muscles that possess complex fibre bundle (FB) geometry (e.g. flexor digitorum superficialis; Blemker and Delp 2005). The lack of comprehensive data that describe the complexity of FB arrangements within each muscle limits the ability to improve upon and properly evaluate the models and simulations used to study muscle behaviour (Blemker et al. 2007).

The geometry and spatial relationships of the contractile and connective tissue elements (i.e. musculotendinous architecture) are important determinants of muscle function (Gans and Gaunt 1991; Lieber and Ward 2011). For

example, the arrangement of the FBs and their attachments to tendons, bone and other connective tissue structures determine the force-generating capability of the muscle, as well as the distance and velocity of excursion, and thus the range of force development (Zajac 1989; Gans and Gaunt 1991). The geometry and organisation of FBs are characterised by quantifiable architectural parameters that include fibre bundle length (FBL), pennation angle (PA) and muscle volume (MV). Often, the mean measured values of the FBL and PA of a specific muscle are used to calculate its physiological cross-sectional area (PCSA) as an estimate of that muscle's force-generating capacity (Zajac 1989; Lieber et al. 1992; Murray et al. 2000). Consequently, the methods used to derive muscle architectural parameters are likely to impact the interpretation of a muscle's behaviour and contribution to movement.

Although the capabilities and performance of musculoskeletal simulators have markedly improved with advancements in computational mechanics, the lack of detailed musculotendinous architectural data continues to hinder the accuracy of biomechanical simulations (Blemker and Delp 2005). Architectural parameters that characterise muscle morphology have been quantified in cadaveric and imaging studies. In the cadaveric studies, architectural data typically consist of measurements taken from a limited number of FBs (5–20 FBs sampled per muscle) located on the superficial surface of, rather than

*Corresponding author. Email: jameszhi.li@mail.utoronto.ca

throughout, the MV (Sacks and Roy 1982). As a result, depending on the complexity of the FB arrangement, the existence of architectural variation and/or spatially distinct regions within a muscle may not be captured and incorporated into musculoskeletal models.

In vivo architectural data have been collected using imaging techniques, including ultrasonography (US), computed tomography (CT), magnetic resonance imaging (MRI) and diffusion tensor MRI (dtMRI). US has been used to document FBL and PA, as well as more generalised parameters such as muscle thickness and anatomical cross-sectional area; however, the depth of penetration of the sound waves and the width of the probe limit the utility of US for imaging whole muscle architecture (Ogawa et al. 2012; Kim et al. 2013). Moreover, it is difficult to track and capture the entire length of a FB using US, especially in long parallel-fibred muscle bellies [e.g. brachioradialis (BR)]. Ultimately, US data-sets represent rather superficial, planar views that can be biased by the selected two-dimensional (2D) plane of measurement (Bénard et al. 2009). CT and MRI can provide data for 3D reconstruction of the MV and surface geometry; however, the internal morphology/architecture cannot be captured (Blemker and Delp 2005; Gilles et al. 2006; Holzbaur et al. 2007; Smeulders et al. 2010). dtMRI, combined with tractography, is a newer and promising method for visualising 3D FB architecture within a MV (Levin et al. 2011; Froeling et al. 2012; Schenk et al. 2013). Nonetheless, the high noise-to-data ratio of dtMRI creates artefacts and signal distortions that currently make it difficult to differentiate muscle fibres from connective tissue structures (e.g. aponeuroses, tendons, blood vessels, nerves). The lack of quantitative muscle morphology data, cadaveric and *in vivo*, emphasises the need for more comprehensive evaluations of muscle architecture.

Digitisation and 3D modelling enable the musculotendinous architecture to be captured throughout the volume of cadaveric muscles *in situ*. Using this technique developed in our laboratory, the detailed FB architecture, as well as the extent and location of aponeuroses and tendons, can be documented. Musculotendinous architectural parameters can be quantified from the digitised data using geometric principles (Ravichandiran et al. 2009; Lee et al. 2012). Although our laboratory has previously used digitisation to investigate the architecture of individual muscles in multiple specimens (Kim et al. 2007; Rosatelli et al. 2008; Fung et al. 2009; Fattah et al. 2013), high-resolution digitisation has not been utilised to generate a complete model/architectural database of the musculotendinous structures of an entire anatomical region (e.g. forearm). In addition to information about individual muscles, complete data from a single individual would provide a 3D spatial map of the interrelationships between the musculotendinous units and their skeletal attachments. Such an all-inclusive data-set would be valuable for the creation of

novel, comprehensive models that are capable of more realistic simulations of muscle and limb behaviour.

Therefore, the goals of this study were: (1) to construct a comprehensive digital database of the musculotendinous architecture at the FB level of all 20 forearm muscles from a single human cadaveric specimen; and (2) to quantify the 3D architectural parameters of each muscle of the forearm using geometric principles.

2. Methods

One formalin-embalmed human upper extremity was used for this study (male in 20s). The specimen had normal muscle mass and no evidence of musculoskeletal abnormality, previous surgery or tendon pathology. Digitisation of the musculotendinous anatomy of the forearm was carried out using a MicroScribe™ 3DX Digitizer (0.3 mm accuracy; Immersion Corporation, San Jose, CA, USA), during cadaveric dissection. Ethics approval was received from the University of Toronto Health Sciences Research Ethics Board.

2.1 Dissection and digitisation

The skin and fascia of the forearm and hand were removed. To immobilise the elbow, wrist, carpometacarpal, metacarpophalangeal and interphalangeal joints in a neutral posture, metal plates were anchored across the joints using screws. A single screw was drilled into each of three bony prominences, two in the ulna (ulnar head and olecranon process) and one in the radius (styloid process). These three screws served as reference markers that facilitated the registration and computerised reconstruction of all of the digitised data. Initially, each of the reference markers was sequentially digitised to calibrate the local workspace and to establish a global reference frame. Each marker was then digitised again prior to the digitisation of each muscle, to facilitate reconstruction of the digitised coordinate data from each of the musculotendinous structures into the complete 3D model.

The FBs and aponeurosis/tendon complexes of the 20 forearm muscles were sequentially digitised. Starting from the superficial surface, the FBs of each muscle were digitised throughout the MV, during serial dissection. Each FB was delineated between its attachment sites (Figure 1(A)) and digitised from proximal to distal at 5–10 mm intervals (Figure 1(B)). The FBs were removed after digitisation to expose the underlying FBs. These steps were repeated until all of the FBs for that musculotendon unit had been digitised. During this process, the perimeter and surface of any aponeuroses and internal tendons were also digitised, as they were exposed. To volumetrically document the dimensions of the external tendon (i.e. tendon of insertion) *in situ*, the surface of the tendon was first marked with a series of curves at 5 mm intervals, and then the curves were digitised

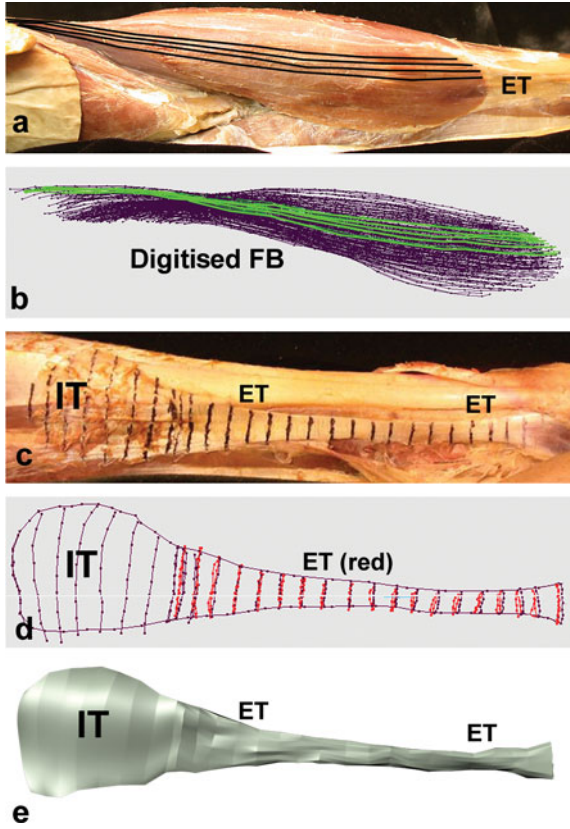


Figure 1. Digitisation of FBs and tendon: (a) delineated FBs are highlighted in black on an embalmed cadaveric specimen; (b) digitised FBs from specimen; (c) preparation for digitization of the tendon: internal part of tendon (IT) and external part of tendon (ET). Curved black lines marked at 5 mm intervals; (d) digitised tendon with cross-sectional circumference placed at the appropriate 5 mm interval markings; (e) tendon reconstructed in 3D using Autodesk[®] Maya[®] with plug-ins developed in our laboratory.

(Figure 1(C)). Next, the external tendon was excised and transversely sectioned at the marked intervals (Figure 1(D)). The circumference of each cross section was then digitised for later 3D reconstruction of the tendon (Figure 1(E)). Once all of the muscles had been digitised and dissected, the remaining osseoligamentous specimen was scanned using a FARO[®] Laser ScanArm[®] (FARO Technologies Inc., Lake Mary, FL, USA).

2.2 3D modelling

The digitised musculotendon data were modelled in the Autodesk[®] Maya[®] software platform (Autodesk Inc., San Rafael, CA, USA) using custom software plug-ins developed in our laboratory. As a pre-process, the path of each digitised FB was approximated by a cubic uniform B-Spline, with clamped boundary conditions, and then stored as a Maya[®] non-uniform rational linear basis spline (NURBS) curve (Ravichandiran et al. 2009). A volumetric reconstruction of these data was generated by extruding each FB curve into a cylindrical tube, which was used to view the FB arrangement

throughout the volume of each muscle. Next, the internal tendon structures were reconstructed in Maya[®] by lofting the curves obtained from the surface of the aponeurosis into NURBS surfaces. To reconstruct the external tendon in 3D, the sites of the incrementally marked curves along the tendon were used to spatially locate the corresponding circumference data. The curves of the circumferential data were then lofted into a surface. This technique allowed the tendon to be reconstructed as it lay intact in relation to the FBs and aponeuroses. Lastly, a surface mesh model of the osseoligamentous specimen of the forearm and hand was constructed using Geomagic Studio[®] 12 (Geomagic, Morrisville, NC, USA). All of the digitised components (e.g. muscles, tendons, bones) were reconstructed and assembled in Maya[®] to construct the complete model of the musculoskeletal elements of the forearm, as situated in the specimen. An iterative closest point algorithm was used to position the reconstructed FB data for each muscle, according to the 3D coordinates of the digitised reference markers.

2.3 Estimation of architectural parameters

Architectural parameters were quantified from the digitised data using custom software. Each digitised FB was initially modelled as a polyline to connect the series of digitised points. To increase the reliability and precision of the quantification process, the polyline was transformed into smooth curves using a catmull-rom spline, $\mathbf{p}(u) = (x(u), y(u), z(u))$, where $u \in [0, 1]$. These curves were uniformly resampled to normalise the spacing between points. The architectural parameters were then quantified based on these spline models. For the purpose of this study, the FBL, MV and PCSA were computed using the method developed by Lee et al. (2012). The PA was computed relative to the muscle's line of action using a new algorithm that is presented below (see Section 2.3.2).

2.3.1 Fibre bundle length

In the spline-based FB model, the length of each curve segment was given by its arc length:

$$l(t) = \int_{t_0}^t \left\| \frac{d\mathbf{p}(u)}{du} \right\| du.$$

To reduce the computational demand, FBs were transformed into smooth curves and the chord length was used to approximate the curve length of each segment:

$$l(u_k) \approx \|\mathbf{p}(u_k) - \mathbf{p}(u_{k-1})\|.$$

Therefore, the entire length of each FB, i , was approximated by

$$\text{FBL}^i = \sum_{k=1}^n \|\mathbf{p}(u_k) - \mathbf{p}(u_{k-1})\|, \quad (1)$$

where $u_0 = 0$ and $u_n = 1$.

2.3.2 Pennation angle

PA is the angle between the orientation of the FB (Equation (3)) and the muscle's line of action (Equation (4) for pennate or Equation (5) for non-pennate muscles).

For each FB^i , its PA was calculated as

$$PA = \cos^{-1}(\text{orientation of } FB^i \cdot \text{line of action}). \quad (2)$$

The orientation of each FB was computed according to a series of tangent vectors that were calculated along each curve, using $\mathbf{p}'(u) = (x'(u), y'(u), z'(u))$. Specifically, tangent vectors were determined at both the proximal and distal attachments ($\mathbf{p}'(0)$ and $\mathbf{p}'(1)$, respectively) and used to compute PA according to (2). To provide a more faithful estimation of the orientation of each FB, an average of tangent fields was obtained over a local area around each FB attachment site. Since the angular difference was observed to be small, we used the linear interpolation method to average the tangent field vectors. For each FB^i , averaged tangent vectors for the proximal, $\bar{\mathbf{t}}_p$, and distal orientation, $\bar{\mathbf{t}}_d$, were calculated as

$$\bar{\mathbf{t}}_p = \frac{1}{n_p} \sum_{u=0}^{u_p} \mathbf{t}(u), \quad \bar{\mathbf{t}}_d = \frac{1}{n_d} \sum_{u=u_d}^1 \mathbf{t}(u), \quad (3)$$

where $\mathbf{t}(u)$ is the tangent vector defined at the point $\mathbf{p}(u)$, and n_p and n_d are the number of points of the proximal and distal regions, respectively, and $u \in [0, \dots, u_p, \dots, u_d, \dots, 1]$. In this study, we chose a range of 0.15 – 0.2 for u_p and 0.8 – 0.85 for u_d , indicating that approximately 15 – 20% of the entire FBL was accounted for in the tangent field calculations at both the proximal and distal regions of each FB (Figure 2).

To estimate the effective line of action of the muscle, two separate methods were developed, one for muscles with a pennate FB arrangement and the other for non-pennate muscles. To classify a muscle as pennate or non-pennate, we used a least square regression method to find the line of best fit through the cluster of distal attachment points for all of the digitised FBs from that muscle:

$$\min_{\beta_1, \beta_2} \sum \|s(\mathbf{p}) - \beta_1 t - \beta_2\|^2, \quad (4)$$

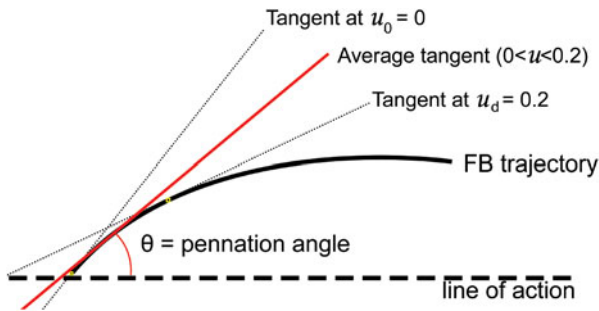


Figure 2. Schematic of PA calculation. The directionality of a FB was approximated using the average tangent field of 20% of the FBL from $u_0 = 0$.

where $s(\mathbf{p})$ represents the 3D coordinate data of the distal attachment points of the digitised FBs and $\beta_1 t + \beta_2$ is the regression model used to find the line of best fit to the 3D coordinate data, $s(\mathbf{p})$. The unit vector β_1 describes the principal distribution of distal attachment coordinate points along the distal tendon, which was used to define the line of action.

Quantitatively, a muscle was considered to be pennate when the distal FB attachment sites exhibited strong linearity [i.e. the coefficient of determination (R^2) from the regression analysis was > 0.9]. In contrast, non-pennate (i.e. fusiform and parallel-fibred) muscles exhibited markedly weaker linearity in their internal tendon/distal FB attachment regions. In this study, if the linear regression yielded an R^2 value of < 0.9 , then the β_1 value in Equation (4) was determined to not accurately represent the directionality of the line of action. In the case of non-pennate muscles, the line of action was approximated by taking the averaged direction of collective tangent vectors of all FBs at the distal attachment ($\bar{\mathbf{t}}_d$), within a given muscle, using the following equation:

$$\text{Line of action}_d = \frac{1}{n} \sum_{i=1}^n \bar{\mathbf{t}}_d^i, \quad (5)$$

where n is the number of FBs.

2.3.3 PCSA and MV

The quantification methods for PCSA and MV were described previously by Lee et al. (2012). Briefly, to calculate the PCSA and MV, volumetric information for each FB was recovered from the digitised data. The cross-sectional areas computed for each FB were constrained by its neighbouring bundles. To approximate the cross-sectional area of a FB at a specific location along its length, Voronoi's tessellation was used,

$$V(\mathbf{p}) = \left\{ \mathbf{v} \mid \mathbf{v} = \frac{(\mathbf{q} + \mathbf{p})}{2}, \mathbf{q} \in N(\mathbf{p}) \right\}, \quad (6)$$

where $V(\mathbf{p})$ is a set of points representing the Voronoi region at \mathbf{p} , $N(\mathbf{p})$ is the set of all neighbouring points around Voronoi's site that is represented by \mathbf{p} , and was determined by the intersection of the transverse plane at \mathbf{p} and the neighbouring FBs. In (6), \mathbf{q} is an arbitrary point along the spline curve used to represent the FB. Since a cross section of the FB was adjoined by a finite number of neighbouring FBs, only immediate neighbours were taken into account when calculating the cross-sectional area of that FB. Using Voronoi's tessellation, the cross-sectional area of a FB was approximated by a polygon that was formed by a set of points that were equidistant from \mathbf{p} and its neighbouring FBs \mathbf{q} . Thus, the cross-sectional area, A , at \mathbf{p} , was approximated by the polygon formed by $V(\mathbf{p})$

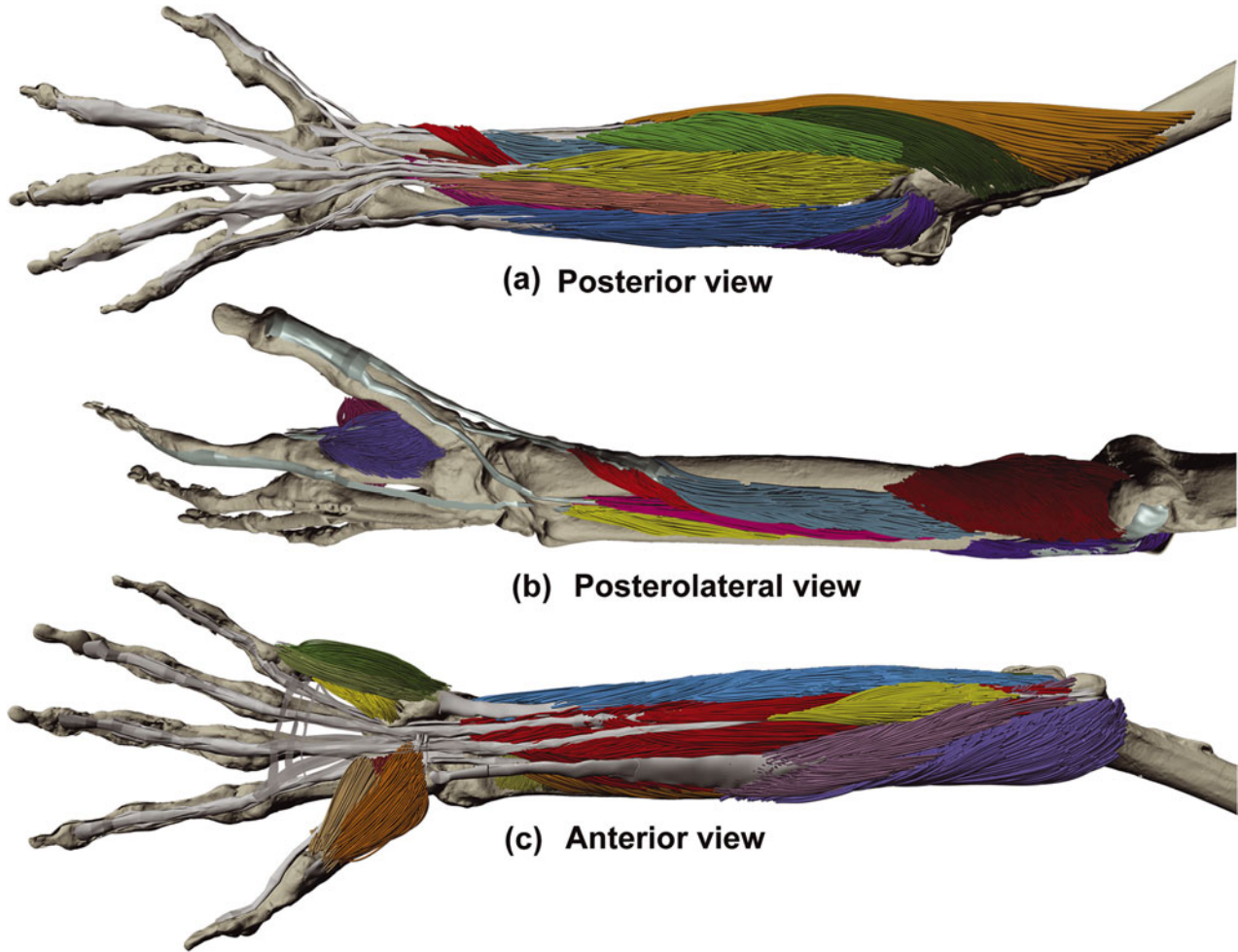


Figure 3. 3D models of forearm relative to the underlying skeleton: (a) posterior muscles of forearm, (b) thumb muscles, (c) anterior muscles of forearm.

(i.e. Voronoi region). The cross-sectional area was calculated along the length of each FB at 1–3 mm intervals and averaged to compute the mean cross-sectional area of the FB. For example, the mean cross-sectional area of one typical FB (length 59.2 mm) in extensor carpi radialis brevis was $0.94 \pm 0.42 \text{ mm}^2$. The mean cross-sectional area of each FB was used to calculate the PCSA of the muscle, taking into consideration the PA

measured relative to the distal line of action (2). The PCSA was calculated as

$$\text{PCSA} = \sum_{i=1}^n \bar{A}_i \cos(\text{PA}^i), \quad (7)$$

where \bar{A}_i is the mean cross-sectional area of FB^i and n is the number of FBs and PA was obtained from (2).

Table 1. Summary of architectural parameters of selected muscles.

Muscle	nFB	FBL (mm)	PA (°)	PCSA (mm ²)	MV (cm ³)
BR	182	205.4 ± 26.3	2.9 ± 2.0	278.3	56.1
PT	1218	44.3 ± 12.9	21.6 ± 6.5	790.0	36.0
EPL	201	53.8 ± 5.4	6.5 ± 3.1	131.1	7.1
FDP	1604	77.1 ± 9.7	9.0 ± 4.6	1102.2	85.0
FCU	1047	40.3 ± 14.5	15.5 ± 7.0	631.9	26.8
SP	1280	25.3 ± 5.5	21.0 ± 12.0	1074.2	32.4

Notes: nFB, number of fibre bundles sampled; FBL, fibre bundle length (average); PA, pennation angle (average, distal); PCSA, physiological cross-sectional area; MV, muscle volume.

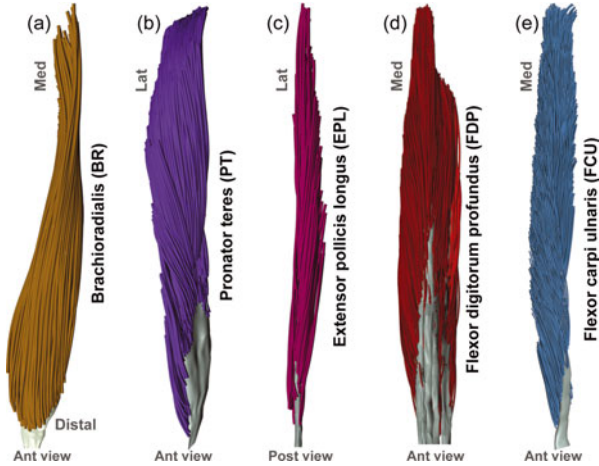


Figure 4. 3D computer models of (a) brachioradialis, (b) PT, (c) EPL, (d) FDP, (e) FCU. Lat, lateral; Med, medial; Ant, anterior; Post, posterior.

Finally, the volume of each FB was obtained by multiplying \bar{A}_i of that FB by its FBL; therefore, the volume of all FBs in a muscle, or MV, was approximated by

$$\text{Volume} = \sum_{i=1}^n \bar{A}_i \text{FBL}^i. \quad (8)$$

Architecturally distinct regions were initially identified by visual inspection of the 3D model and verified by the parameter data (FBL, PA and attachment sites).

3. Results

Once compiled into the 3D model, the complete forearm muscle database demonstrated variation in the size and architectural complexity of the 20 forearm muscles *in situ*, both visually (Figure 3) and geometrically (Table 1). In

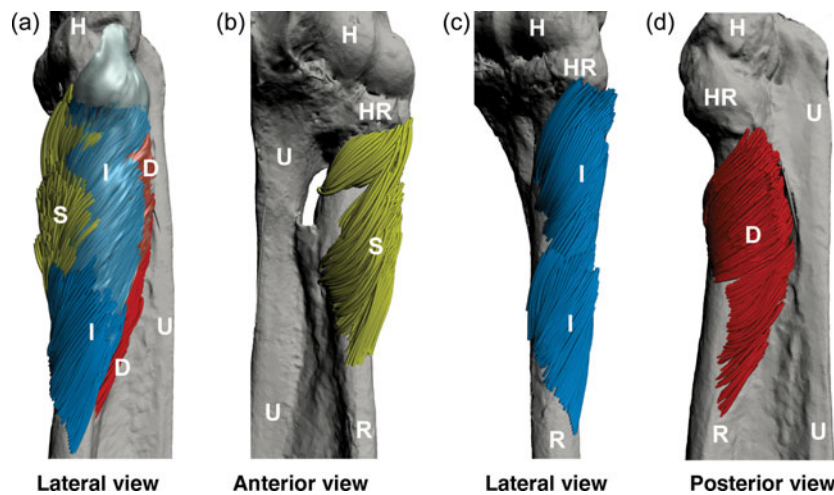


Figure 5. 3D computer model of SP: (a) whole muscle, lateral view; (b) superficial part (S); (c) intermediate part (I); (d) deep part (D). H, humerus; HR, head of radius; R, radius; U, ulna.

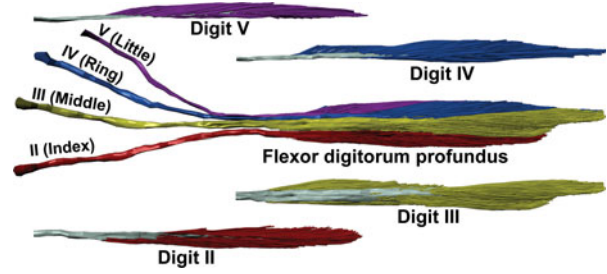


Figure 6. 3D computer model of the digital belly of FDP.

total, 14,427 FBs were digitised. Based on muscle size and the complexity of FB trajectories, between 150 (extensor pollicis brevis) and 2100 (flexor digitorum superficialis) FBs per muscle were digitised throughout their entire volume. Also, the external tendon(s) of insertion for each muscle were reconstructed volumetrically using the digitised cross-sectional data. The digitisation of the entire forearm was a time-intensive process that required 12–60 h to meticulously dissect and digitise each muscle, depending on its size and complexity.

Six muscles with different sizes, shapes and internal structures were selected to illustrate the morphological variation in the forearm musculature (Figures 4 and 5): the long, strap-like BR and flexor carpi ulnaris (FCU); the pronator teres (PT) and supinator (SP) antagonistic forearm rotators; and the extensor pollicis longus (EPL) and flexor digitorum profundus (FDP) as examples of digital muscles.

Despite their similar superficial morphological appearance, the BR and FCU varied greatly in internal structure. The long parallel FBs of BR spanned the length of the muscle, whereas the FCU consisted of shorter FBs that have a larger PA (Figure 4 and Table 1). This is reflected in the PCSA of FCU, which is almost double that of BR, despite FCU having a markedly smaller volume.

Table 2. Summary of architectural parameters of digital bellies of FDP.

Parameters	All digits	II	III	IV	V
nFB	1604	445	544	321	294
FBL (mm)	76.9 ± 9.7	65.3 ± 3.9	83.7 ± 6.7	82.6 ± 6.3	76.0 ± 6.4
PA (°)	9.0 ± 4.6	10.8 ± 4.2	7.5 ± 3.5	7.4 ± 4.7	10.8 ± 5.0
PCSA (mm ²)	1100.1	353.6	374.1	195.8	176.6
MV (cm ³)	84.6	23.5	31.3	16.1	13.7

Notes: nFB, number of fibre bundles sampled; FBL, fibre bundle length (average); PA, pennation angle (average, distal); PCSA, physiological cross-sectional area; MV, muscle volume.

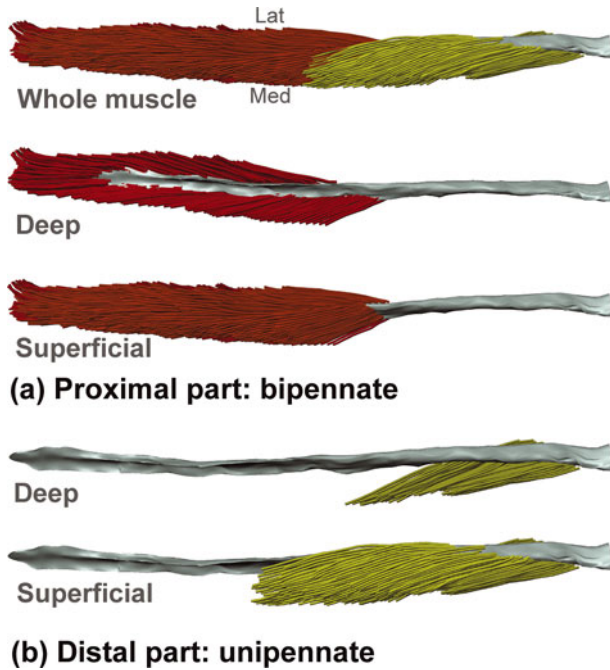


Figure 7. 3D computer model of parts of FCU: (a) proximal part and (b) distal part. Lat, lateral; Med, medial.

The FB arrangement of both the PT and SP muscles was complex, yet distinctively different (Figures 4(b) and 5). Visual examination showed that the PT is an obliquely oriented cylindrical shaped muscle, whereas the SP spirals around the radius. Although the average PAs of the two muscles were virtually identical, the average FBL of PT was approximately 20 mm longer than that of the SP

Table 3. Architectural parameters of parts of FCU.

Parameters	Proximal	Distal
nFB	822	225
FBL (mm)	39.9 ± 3.3	41.4 ± 4.9
PA (°)	14.3 ± 6.0	19.9 ± 8.4
PCSA (mm ²)	481.0	150.6
MV (cm ³)	19.8	6.8

Notes: nFB, number of fibre bundles sampled; FBL, fibre bundle length (average); PA, pennation angle (average, distal); PCSA, physiological cross-sectional area; MV, muscle volume.

muscle. Despite similar volumes, the PCSA of SP was about 1.4 times larger than PT (Table 1).

The FDP and EPL differed in their visual morphology and also varied in their architecture (Figure 4 and Table 1). From the muscle surface, the individual subdivisions of the FDP belly for each finger could not be visualised. In comparison with the FDP (across digits), the volume of EPL was nearly 12 times smaller, and the average FBL was about 25 mm shorter. Consequently, the overall PCSA of FDP was calculated to be approximately eight times greater than that of EPL (Table 1).

The combination of the 3D model and the architectural database enabled instances of architecturally distinct regions to be identified within the volumes of some muscles. Individual subdivisions of FDP which attach to the tendons of digits 2–5 each had unique architectural parameters (Figure 6, Table 2), with no two parts having the same FB arrangement. Specifically, the average FBL was shortest for digit 2 belly and longest for digit 3 belly, while the PCSA was smallest in digit 5 belly and largest in digit 3 belly. As another example, the FCU can be further subdivided into an architecturally distinct bipennate part proximally, and a unipennate part distally (Figure 7). Compared with the proximal bipennate part, the distal unipennate part had a larger average PA and less than one-third of the PCSA (Table 3). In addition, the SP muscle was partitioned into three regions based on the distal attachment site: deep, intermediate and superficial (Figure 5(b)–(d)).

4. Discussions

The digital atlas described in this study is the only available database that provides 3D coordinate data of the complete forearm musculotendinous anatomy in relation to the underlying skeleton. Since all FBs were digitised from the same specimen, any architectural differences between muscles were real differences and were not caused or biased by interspecimen variation. The digital format allowed us to quantify and visually examine the intricacies of the spatial relationships between muscles, as well as the 3D arrangement of the FBs in relation to their tendons and aponeuroses. The current data demonstrate that even muscles that appear to be morphologically

simple, from their superficial appearance, can contain considerable variation in architecture throughout their volumes. The tools and techniques implemented in this study enabled us to identify and quantify differences between architecturally distinct regions that are often lumped into a single MV.

The current data demonstrate that the common assumption of architectural homogeneity within a muscle is not representative of the actual FB arrangement in many muscles. Only by digitising a large number of FBs (i.e. minimum of 150) throughout the volume of each muscle was it possible to quantify the range of architectural variability within and between muscles for the same specimen. To illustrate, we used geometric principles to determine that any particular FB ($n = 1218$) within the PT could vary by as much as $\pm 30\%$ of its average FBL and PA (Table 1). This represents more than a threefold greater variation in architectural parameters within a single muscle than has been reported for the same muscle across multiple specimens (Lieber et al. 1992). Importantly, the current 3D coordinate data allowed architectural parameters to be calculated and reported: (1) at the individual FB level, (2) for any region of a particular muscle and (3) for the whole muscle. This is in contrast to much of the previous literature that has generalised FB geometry based on manual measurements of a small number (5–20) of superficially located FBs, using tools that only provide 2D information (An et al. 1981; Brand et al. 1981; Lieber et al. 1992; Murray et al. 2000). The range of architectural heterogeneity determined in this study expands upon existing architectural data-sets, and demonstrates the true complexity of forearm muscle design.

The greatest heterogeneity of the FB geometry occurred in instances in which muscles comprised architecturally distinct regions. Specifically, SP was divided into three regions (superficial, intermediate and deep), each comprising its own unique architecture. In addition, FCU was divided into a proximal bipennate part and a distal unipennate part. Based on the FB arrangement of FCU, the bipennate component would generate force on the central tendon in a manner different from the distal unipennate region, which only attached to the medial side of the tendon (Figure 7). These findings could hold functional relevance within a biomechanical context. For example, the distinct regions of the FCU may play an important functional role in the kinematics of the pisiform bone (Moojen et al. 2001), whereby force transmission can be controlled according to the anatomical plane in which wrist movement or stabilisation is desired (Jones et al. 1993; Segal et al. 2002). These features of muscle behaviour would likely be lost in a muscle model that treated architecturally heterogeneous muscles as a single, lumped volume. The existence of data that describe distinct architectural regions in the various muscles creates an important resource for those attempting to better understand force transmission and muscle function.

The combination of techniques applied in this study enabled us to quantify muscle architectural parameters at a greater resolution than is currently possible using imaging methods. For example, based on our calculations of FB cross-sectional areas, we were able to digitise FBs and aponeuroses throughout each MV at sub-millimetre resolution. A major trade-off to obtain data of such resolution was the time-intensive nature of the serial dissection and digitisation. Although dtMRI has shown promise for the non-invasive reconstruction of muscle fibre architectures, direct comparisons with cadaveric dissections and digitised data have revealed that dtMRI often intersperses FB geometries that are non-physiological (Froeling et al. 2012; Schenk et al. 2013). This likely relates to difficulties in properly defining diffusivity parameters and points to the problem of how one chooses an appropriate fibre direction at each voxel given a potentially noisy tensor field (Levin et al. 2011). Filtering techniques can be used to denoise dtMRI data, and thus generate more ‘anatomically plausible’ fibre architectures (Levin et al. 2011); however, how much ‘real’ detail can be removed before it becomes unacceptable remains unclear. The volumetric, comprehensive data-sets obtained in this study could be used for validation of dtMRI data-sets and for the development of tractography algorithms to identify non-physiological geometry within a noisy tensor field, as well as to delineate FBs from other internal structures (e.g. intramuscular tendons).

By capturing the spatial arrangement of the FBs throughout the volume of each muscle, we have compiled a data-set from which multi-resolution musculotendinous models can be generated. From this musculotendinous database, tangent field vectors can be obtained for any muscle in the data-set, whether calculated to represent the entire muscle or distinct regions of a particular muscle. In this way, we anticipate value when representing muscles using line-based models and strand methods to estimate the effective lines of action (Van der Helm and Veenbaas 1991; Holzbaaur et al. 2005; Sueda et al. 2008; Wohlman and Murray 2013). Moreover, the current data will benefit the generation of more realistic finite element (FE) representations of individual FBs to be incorporated. This could markedly improve previous FE muscle models that inferred the internal arrangement of the muscle fibres by assuming some level of architectural homogeneity within a volumetric mesh (Blemker and Delp 2005; Stavness et al. 2012). By creating *in situ* FB geometry templates, the current data could be morphed into a subject-specific volumetric mesh using a frame-based deformation field technique (Gilles et al. 2011). In future studies, gender, age and physical build of subjects will need to be considered to increase the inter-subject variability of the database. By improving the comprehensiveness of the data that are used to generate musculotendinous models, the biomechanics

community can move towards better predictions of overall muscle behaviour (e.g. deformation, range of force development and excursion), and thus a better understanding of muscle force transmission and muscle function.

Acknowledgements

The authors wish to gratefully thank the Natural Sciences and Engineering Research Council (NSERC) and Autodesk Research Inc. for their generous support and the other members of the Parametric Human research group for their discussions and insights. The authors greatly appreciate the assistance of William Wood, technical staff of the Division of Anatomy, Department of Surgery. The authors also wish to thank the individuals who donated their bodies and tissue for the advancement of education and research.

Notes

1. Email: jeremy.mogk@autodesk.com
2. Email: dwlee@cs.toronto.edu
3. Email: jacky.bibliowicz@autodesk.com
4. Email: anne.agur@utoronto.ca

References

- An KN, Hui FC, Morrey BF, Linscheid RL, Chao EY. 1981. Muscles across the elbow joint: a biomechanical analysis. *J Biomech.* 14(10):659–669.
- Bénard MR, Becher JG, Harlaar J, Huijting PA, Jaspers RT. 2009. Anatomical information is needed in ultrasound imaging of muscle to avoid potentially substantial errors in measurement of muscle geometry. *Muscle Nerve.* 39(5):652–665.
- Blemker SS, Asakawa DS, Gold GE, Delp SL. 2007. Image-based musculoskeletal modeling: applications, advances, and future opportunities. *J Magn Reson Imaging.* 25(2):441–451.
- Blemker SS, Delp SL. 2005. Three-dimensional representation of complex muscle architectures and geometries. *Ann Biomed Eng.* 33(5):661–673.
- Brand PW, Beach RB, Thompson DE. 1981. Relative tension and potential excursion of muscles in the forearm and hand. *J Hand Surg Am.* 6(3):209–219.
- Fattah AY, Ravichandiran K, Zuker RM, Agur AM. 2013. A three-dimensional study of the musculotendinous and neurovascular architecture of the gracilis muscle: application to functional muscle transfer. *J Plast Reconstr Aesthet Surg.* 66(9):1230–1237.
- Froeling M, Nederveen AJ, Heijtel DF, Lataster A, Bos C, Nicolay K, Maas M, Drost MR, Strijkers GJ. 2012. Diffusion-tensor MRI reveals the complex muscle architecture of the human forearm. *J Magn Reson Imaging.* 36(1):237–248.
- Fung L, Wong B, Ravichandiran K, Agur A, Rindlisbacher T, Elmaraghy A. 2009. Three-dimensional study of pectoralis major muscle and tendon architecture. *Clin Anat.* 22(4):500–508.
- Gans C, Gaunt AS. 1991. Muscle architecture in relation to function. *J Biomech.* 24(Suppl. 1):53–65.
- Gilles B, Bousquet G, Faure F, Pai DK. 2011. Frame-based elastic models. *ACM Trans Graph.* 30(2):15 (12 pages).
- Gilles B, Moccozet L, Magnenat-Thalmann N. 2006. Anatomical modelling of the musculoskeletal system from MRI. *Med Image Comput Comput Assist Interv.* 9(Pt 1):289–296.
- Holzbaur KR, Murray WM, Delp SL. 2005. A model of the upper extremity for simulating musculoskeletal surgery and analyzing neuromuscular control. *Ann Biomed Eng.* 33: 829–840.
- Holzbaur KR, Murray WM, Gold GE, Delp SL. 2007. Upper limb muscle volumes in adult subjects. *J Biomech.* 40(4): 742–749.
- Jones KE, Bawa P, McMillan AS. 1993. Recruitment of motor units in human flexor carpi ulnaris. *Brain Res.* 602:354–356.
- Kim SY, Bleakney RR, Rindlisbacher T, Ravichandiran K, Rosser BW, Boynton E. 2013. Musculotendinous architecture of pathological supraspinatus: a pilot *in vivo* ultrasonography study. *Clin Anat.* 26(2):228–235.
- Kim SY, Boynton EL, Ravichandiran K, Fung LY, Bleakney RR, Agur AM. 2007. Three-dimensional study of the musculotendinous architecture of supraspinatus and its functional correlations. *Clin Anat.* 20(6):648–655.
- Lee D, Ravichandiran K, Jackson K, Fiume E, Agur A. 2012. Robust estimation of physiological cross-sectional area and geometric reconstruction for human skeletal muscle. *J Biomech.* 45(8):1507–1513.
- Lee SH, Sifakis E, Terzopoulos D. 2009. Comprehensive biomechanical modeling and simulation of the upper body. *ACM Trans Graph.* 28(4):1–17.
- Levin DIW, Gilles B, Mädler B, Pai DK. 2011. Extracting skeletal muscle fiber fields from noisy diffusion tensor data. *Med Image Anal.* 15(3):340–353.
- Lieber RL, Jacobson MD, Fazeli BM, Abrams RA, Botte MJ. 1992. Architecture of selected muscles of the arm and forearm: anatomy and implications for tendon transfer. *J Hand Surg Am.* 17(5):787–798.
- Lieber RL, Ward SR. 2011. Skeletal muscle design to meet functional demands. *Philos Trans R Soc Lond B Biol Sci.* 366(1570):1466–1476.
- Moojen TM, Snel JG, Ritt MJ, Venema HW, den Heeten GJ, Bos KE. 2001. Pisiform kinematics *in vivo*. *J Hand Surg Am.* 26(5):901–907.
- Murray WM, Buchanan TS, Delp SL. 2000. The isometric functional capacity of muscles that cross the elbow. *J Biomech.* 33(8):943–952.
- Ogawa M, Mitsukawa N, Bembem MG, Abe T. 2012. Ultrasound assessment of adductor muscle size using muscle thickness of the thigh. *J Sport Rehabil.* 21(3):244–248.
- Ravichandiran K, Ravichandiran M, Oliver ML, Singh KS, McKee NH, Agur AM. 2009. Determining physiological cross-sectional area of extensor carpi radialis longus and brevis as a whole and by regions using 3D computer muscle models created from digitized fiber bundle data. *Comput Methods Programs Biomed.* 95(3):203–212.
- Rosatelli AL, Ravichandiran K, Agur AM. 2008. Three-dimensional study of the musculotendinous architecture of lumbar multifidus and its functional implications. *Clin Anat.* 21(6):539–546.
- Sacks RD, Roy RR. 1982. Architecture of the hindlimb muscles of cats: Functional significance. *J Morphol.* 173(2):185–195.
- Schenk P, Siebert T, Hiepe P, Güllmar D, Reichenbach JR, Wick C, Blickhan R, Böl M. 2013. Determination of three-dimensional muscle architecture: validation of the DTI-based fibre tractography method by manual digitization. *J Anat.* 223(1):61–68.

- Segal RL, Catlin PA, Krauss EW, Merick KA, Robilotto JB. 2002. Anatomical partitioning of three human forearm muscles. *Cells Tissues Organs*. 170(2–3):183–197.
- Smeulders MJ, van den Berg S, Oudeman J, Nederveen AJ, Kreulen M, Maas M. 2010. Reliability of *in vivo* determination of forearm muscle volume using 3.0 T magnetic resonance imaging. *J Magn Reson Imaging*. 31(5):1252–1255.
- Stavness I, Lloyd JE, Fels S. 2012. Automatic prediction of tongue muscle activations using a finite element model. *J Biomech*. 45(16):2841–2848.
- Sueda S, Kaufman A, Pai DK. 2008. Musculotendon simulation for hand animation. *ACM Trans Graph*. 27(3):83 (8 pages).
- Van der Helm FC, Veenbaas R. 1991. Modelling the mechanical effect of muscles with large attachment sites: application to the shoulder mechanism. *J Biomech*. 24(12):1151–1163.
- Wohlman SJ, Murray WM. 2013. Bridging the gap between cadaveric and *in vivo* experiments: a biomechanical model evaluating thumb-tip endpoint forces. *J Biomech*. 46(5):1014–1020.
- Zajac FE. 1989. Muscle and tendon: properties, models, scaling, and application to biomechanics and motor control. *Crit Rev Biomed Eng*. 17(4):359–411.